Dirac points and topological phases in correlated altermagnets

Lorenzo Del Re*
Max-Planck-Institute for Solid State Research, 70569 Stuttgart, Germany
and Institut für Theoretische Physik und Astrophysik and Würzburg-Dresden Cluster of Excellence ct.qmat, Universität Würzburg, 97074 Würzburg, Germany

(Received 4 September 2024; accepted 11 August 2025; published 10 September 2025)

We explore a two-dimensional Hubbard model adapted to host altermagnetic states. Utilizing Hartree-Fock (HF) and dynamical mean-field theory (DMFT), we uncover that the magnetic solutions of this model feature Dirac points in their spectrum. HF predicts a gap opening at a critical interaction strength, a result corroborated by DMFT calculations at zero temperature. However, at finite temperature and high interaction strengths, Dirac points re-emerge at high energies in the spectral function, even if they are absent in the noninteracting and HF-predicted band structures. Analytical arguments reveal that this phenomenon arises near Mott insulating solutions from the frequency dependence of the self-energy, a behavior not captured by static mean-field theory. We identify distinctive dynamical signatures of correlated altermagnetic states in the spin-resolved optical conductivity, notably a double-peak structure likely linked to high-energy Dirac conelike bands. Moreover, the spin-resolved response exhibits spin-selective activation at different photon energies, pointing to potential applications in spin-dependent optical control. We also propose perturbations to the model that can induce a topological gap in the spectrum, leading to a transition from topologically trivial to nontrivial states by varying doping, interaction strength, and temperature.

DOI: 10.1103/7nvm-s225

I. INTRODUCTION

Many-electron systems can organize in a multitude of magnetically ordered states by spontaneous symmetry breaking. Recently, another type of magnetic order, i.e., altermagnetism [1–8], has been established as a separate category of broken-symmetry phases. Similar to antiferromagnets, altermagnets have a net zero magnetization. However, unlike antiferromagnets, the spin-up and spin-down sublattices are not connected by a simple sublattice translation. This implies a splitting of spin-up/down bands resulting in spin-resolved anisotropic transport properties with potential application in antiferromagnetic (AFM) spintronics [9,10]. Even if experiments and *ab initio* studies on real materials have already found good candidates for hosting altermagnetic states [11–20], cold atoms trapped in optical lattices represent an alternative route for their realization. Furthermore, since cold-atomic setups have been employed for the simulation of strongly correlated Mott insulators [21–24] and quantum magnetism [25–28], they represent the ideal testbed for understanding the interplay between electronic correlations and the emergence of altermagnetism in many fermion systems.

In this work, we study a two-dimensional version of the Hubbard model suitably modified for hosting altermagnetic states that can be simulated via nowadays available cold-atom technology [29]. Here, by employing Hartree-Fock (HF) and dynamical mean-field theory (DMFT) [30], we reveal that magnetic solutions of this model host Dirac points in its spectrum and study their stability as a function of relevant physical parameters such as interaction, doping, and temperature. In particular, HF predicts a gap opening for a critical value of the interaction strength, which is confirmed by our DMFT calculations at zero temperature. At finite temperature and sufficiently strong interaction strength, DMFT predicts the re-emergence of Dirac points at high energy in the spectral function, which are absent in both the noninteracting and HF-predicted band structures. By means of an approximation valid at strong coupling, we analytically show that this phenomenon stems from the frequency dependence of the self-energy in the vicinity of Mott insulating solutions and it is not captured by static mean-field theory. We also investigate the optical conductivity as a probe of the underlying electronic structure in correlated altermagnetic states. Motivated by the presence of high-energy Dirac conelike features at finite temperature and doping, we analyze the spin-resolved dynamical response to an external electric field. This allows us to identify spectroscopic fingerprints—such as a characteristic double-peak structure in the optical conductivity—that are sensitive to spin polarization and band structure. These features not only provide insights into the many-body physics of the system but also suggest experimentally accessible signatures and possible routes toward spin-selective optical manipulation in strongly correlated materials. Finally, we propose perturbations to the model that can open a topological gap in the spectrum. Since

*Contact author: l.delre@fkf.mpg.de; lorenzo.re@uni-wuerzburg.de

Published by the American Physical Society under the terms of the Creative Commons Attribution 4.0 International license. Further distribution of this work must maintain attribution to the author(s) and the published article's title, journal citation, and DOI. Open access publication funded by Max Planck Society.

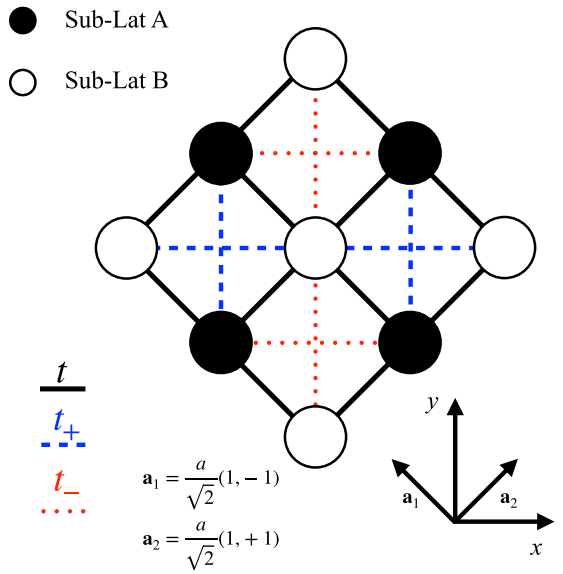


FIG. 1. Sketch of the tight-binding model described in Eq. (1), where $t_\pm = t'(1 \pm \delta)$. The reference frame is aligned with the primary (x) and secondary (y) diagonals. The lattice constant is set to $a = 1/\sqrt{2}$.

the topological states [31–34] are inherently connected to the presence of Dirac points in the unperturbed Hamiltonian, the perturbed system undergoes a transition from topologically trivial to nontrivial by varying doping, interaction strength, and temperature.

II. THE MODEL

We consider the Hubbard model in the square lattice with nearest and next-to-the-nearest neighbor hopping (n.n. and n.n.n., respectively):

$$H = \sum_{ij\sigma} t_{ij} c^\dagger_{i\sigma} c_{j\sigma} + U \sum_i \left(n_{i\uparrow} - \frac{1}{2}\right)\left(n_{i\downarrow} - \frac{1}{2}\right), \qquad (1)$$

where the n.n.n. hopping processes depend explicitly on the sublattice index and assume different values along the main and secondary diagonals, i.e., $t_{\text{n.n.n.}} = -t'[1 + (-1)^a \pm \delta]$ for the main (secondary) diagonal, where $a = A, B$ is the sublattice index [29,35,36] (see Fig. 1).

Such a hopping process explicitly breaks translational invariance and the system must be addressed by adding sublattice indices even in the nonmagnetic phase.

III. HARTREE-FOCK

If we employ a mean-field decoupling of the interactions, the problem is simplified to the following 2×2 Hamiltonian:

$$\mathcal{H}_\sigma(k) = \alpha_k \sigma_0 + \beta_k \sigma^{(z)} + \gamma_k \sigma^{(x)}, \qquad (2)$$

where $\sigma^{(i=x,y,z)}$ are the Pauli matrices, σ_0 is the 2×2 identity matrix, $\alpha_k = [f_A(k) + f_B(k)]/2$, $\beta_k = [f_A(k) - f_B(k) - 2\sigma\Delta]/2$, $\gamma_k = \epsilon_k$, $\epsilon_k = -2t\cos[(k_x + k_y)/2] - 2t\cos[(k_x - k_y)/2)]$ being the n.n., and $f_a = -2t'[1 + (-1)^a\delta]\cos(k_x) - 2t'[1 - (-1)^a\delta]\cos(k_y)$. Here, $\Delta = Um/2$ is the Hartree term coming from the interaction, with $m = n_{A\uparrow} - n_{A\downarrow}$ being the staggered magnetization.

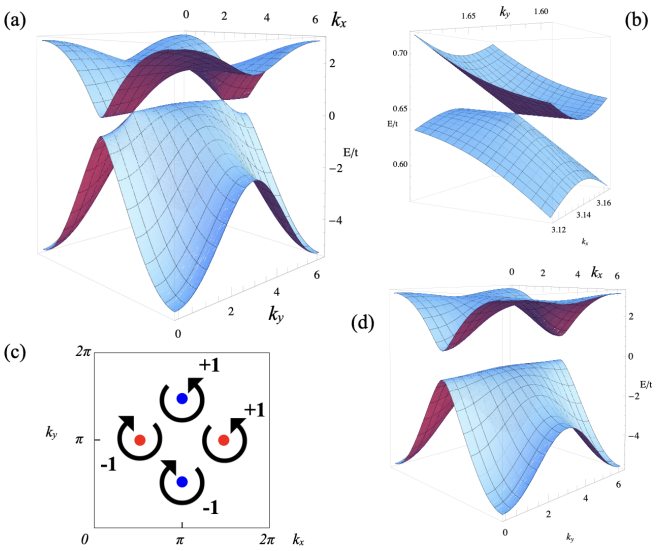


FIG. 2. (a) Band structure for $\sigma = \uparrow$ plotted in the Brillouin zone for $t'/t = 0.3$, $\delta = 0.9$, and $\Delta/t = 3/4 < \Delta_c$. (b) Inset of panel (a) around one of the two crossing points showing the tilted type-I Dirac cone. (c) Positions of the crossing points in the Brillouin zone for $\sigma = \uparrow$ (blue) and $\sigma = \downarrow$ (red) for the same parameter set as in panel (a). The spin-resolved Dirac points possess opposite winding numbers $W = \pm 1$ (indicated by arrows). (d) Gapped band structure for $\sigma = \uparrow$ plotted in the Brillouin zone for $t'/t = 0.3$, $\delta = 0.9$, and $\Delta/t = 7/4 > \Delta_c$.

Dirac cones

The eigenvalues of Eq. (2) read $\lambda^\pm_\sigma(k) = \alpha_k \pm \sqrt{\beta_k^2 + \gamma_k^2}$. The two bands display a crossing when β_k and γ_k simultaneously vanish.

Assuming $\Delta, t', \delta > 0$, the band crossings occur at

$$k_x = \pi, k_y = \pm \arccos\left(\frac{\Delta}{2t'\delta} - 1\right) \quad \text{for } \sigma = \uparrow,$$
$$k_y = \pi, k_x = \pm \arccos\left(\frac{\Delta}{2t'\delta} - 1\right) \quad \text{for } \sigma = \downarrow. \qquad (3)$$

Let us note that there exists a critical value for the order parameter $\Delta_c = 4t'\delta$, such that when $\Delta < \Delta_c$, the bands display a crossing, otherwise they are fully gapped. In Fig. 2(a), the band structure for $t' = 0.3t$, $\delta = 0.9$, and $\Delta = (3/4)t < \Delta_c$ is shown in the Brillouin zone: There are two crossing points per spin species where the two bands form tilted Dirac cones [37] [see inset in Fig. 2(b)]. When $\Delta > \Delta_c$, the two bands are fully gapped as shown in Fig. 2(d).

If the Hamiltonian in Eq. (2) for the $\sigma = \uparrow$ species is expanded around the points defined in Eq. (3), for $\Delta < \Delta_c$, we obtain the following low-energy effective theory:

$$\mathcal{H}^\pm_\uparrow \sim (E_0 + \tilde{v}_y q_y)\sigma_0 \pm v_y q_y \sigma^{(z)} + v_x q_x \sigma^{(x)}, \qquad (4)$$

where $E_0 = -2t'[\cos(\bar{k}_y) - 1]$, $\tilde{v}_y = 2t'\sin(\bar{k}_y)$, $v_x = 2t\cos(\bar{k}_y/2)$, $v_y = -2t'\delta\sin(\bar{k}_y)$, with $\bar{k}_y = \arccos(\Delta/2t'\delta - 1)$, and $\mathbf{q} = (k_x - \pi, k_y \mp \bar{k}_y)$.

The winding vector of Eq. (4) is defined as

$$\mathbf{W} = \frac{1}{2\pi} \oint_{\mathcal{C}} \mathbf{n}(\mathbf{q}) \times d\mathbf{n}(\mathbf{q}), \tag{5}$$

where $\mathbf{n}(\mathbf{q}) = \mathbf{h}(\mathbf{q})/|\mathbf{h}(\mathbf{q})|$, with $\mathbf{h}(\mathbf{q}) = (v_x q_x, 0, \pm v_y q_y)$, and $\mathcal{C}$ is a closed curve around the crossing point. The two crossing points possess nonvanishing and opposite winding numbers $\mathbf{W} = (0, \pm 1, 0)$ (see Fig. 2).

IV. DMFT

In DMFT [30], the original lattice model is mapped onto an effective Anderson impurity model (AIM) that we solved numerically using exact diagonalization (ED). As a minimal choice for describing the altermagnetic state, we assume a local self-energy, which is diagonal in sublattice and spin indices $\Sigma_{aa',\sigma\sigma'}(\nu) = \delta_{\sigma\sigma'}\delta_{aa'}\Sigma_{\sigma a}(\nu)$ and has the following property: $\Sigma_{\sigma a}(\nu) = \Sigma_{\bar{\sigma}\bar{a}}(\nu)$. Therefore, there are only two independent self-energy components: i.e., $\Sigma_{\uparrow A}(\nu) \equiv \Sigma_{\uparrow}(\nu)$ and $\Sigma_{\downarrow A} \equiv \Sigma_{\downarrow}(\nu)$. Given these assumptions, the Dyson equation for the $\sigma = \uparrow$ species reads

$$G_{\uparrow}^{-1}(k, \nu) = \begin{pmatrix} \zeta_{\uparrow}(\nu) - f_A(\mathbf{k}) & \epsilon_k \\ \epsilon_k & \zeta_{\downarrow}(\nu) - f_B(\mathbf{k}) \end{pmatrix}, \tag{6}$$

where $\zeta_\sigma(\nu) = i\nu + \mu - \Sigma_\sigma(\nu)$ [30,38–43].

The self-consistency equation for $\mathcal{G}_0$ is obtained using the inverse Dyson equation, i.e., $\mathcal{G}_{0,\uparrow}^{-1}(\nu) = G_{\mathrm{loc},\uparrow}^{-1}(\nu) + \Sigma_{\uparrow}(\nu)$, where $G_{\mathrm{loc},\uparrow}(\nu) = (1/V)\sum_k G_{AA,\uparrow}(k, \nu)$. In practice, an initial guess for $\mathcal{G}$ defines the AIM at the first iteration, then the self-energy is extracted using ED, and the Weiss field is updated using the self-consistency condition. The DMFT cycle iterates until convergence of the Weiss field [44].

A. Paramagnetic solution

In the symmetric nonmagnetic phase, $\Sigma_\uparrow = \Sigma_\downarrow$ and the staggered magnetization vanishes. Within this phase, the system is expected to undergo a metal-to-insulator transition upon increasing the on-site interaction at filling $n = 1$. In the upper panel of Fig. 3, we show the imaginary part of the Green's function plotted as a function of the Matsubara frequencies ν. For $U < 12t$, we observe that the imaginary part is finite at the lowest Matsubara frequency, which indicates a metallic behavior. Conversely, for $U = 12t$, the imaginary part vanishes linearly in the limit of $\nu \to 0^+$, which signals a vanishing spectral weight at the Fermi level and the opening of a gap. From the knowledge of the self-energy, we can extract the quasiparticle (QP) weight $Z_{\mathrm{q.p.}} = (1 - \partial_\omega \Sigma|_{\omega=0})^{-1}$, which measures the degree of correlation in the metallic state. The lower panel of Fig. 3 shows $Z_{\mathrm{q.p.}}$ as a function of the interaction at fixed density $n = 1$, for $t' = 0.3t$ and $\delta = 0.9$.For this numerical dataset and the ones shown in the remainder of this paper, the number of bath sites has been fixed to $N_b = 5$.

B. Magnetic solution

Magnetic solutions are obtained by relaxing the SU(2) symmetry constraints and allowing $\Sigma_\uparrow$, $\Sigma_\downarrow$ to take independent values. We studied the system by varying doping, interaction, and temperature, and we find four main kinds of

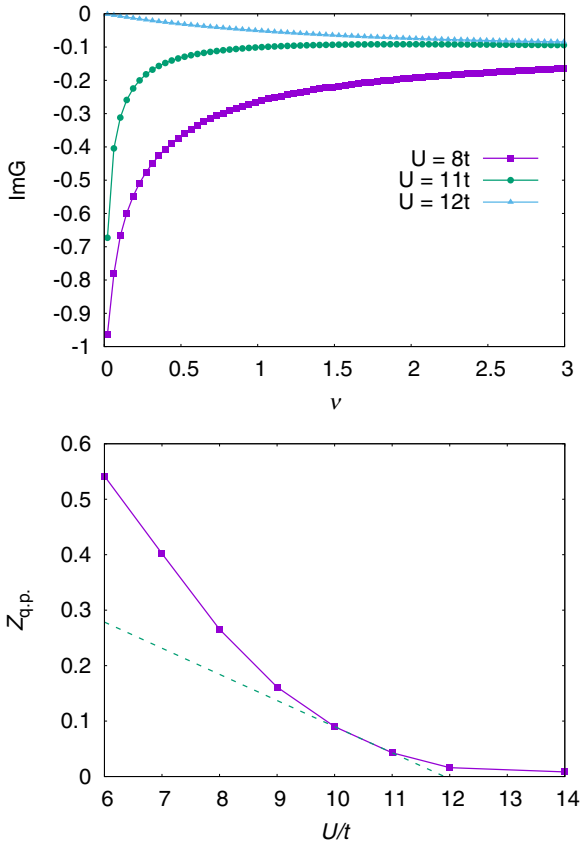


FIG. 3. (Top panel) Imaginary part of the electronic Green's function evaluated on the imaginary frequencies $\nu = (2n+1)\pi/\beta$ for three different values of $U/t = 8,\ 11,\ 12$. (Lower panel) Quasiparticle weight as a function of on-site interaction at integer filling. The dashed line has been obtained from a linear extrapolation of the last two metallic solutions at $U/t = 10,\ 11$. The other parameters for both panels are given by $t'/t = 0.3$ and $\delta = 0.9$.

solutions with broken symmetry: (1) fully gapped insulating AFM without Dirac cones; (2) a magnetic metallic phase obtained by doping the fully gapped one without Dirac cones; (3) a magnetic metallic phase with Dirac cones; and (4) an insulating magnetic phase with high-energy Dirac cones. All these phases display the particular feature of altermagnets, i.e., a lifted spin degeneracy in the single-particle spectrum.

1. Zero temperature

In Fig. 4, we show the density $n = n_{A\uparrow} + n_{A_\downarrow}$ and staggered magnetization $m = n_{A\uparrow} - n_{A_\downarrow}$ curves as a function of the chemical potential for two different values of $U/t = 6, 8$ at zero temperature and for $t'/t = 0.3$ and $\delta = 0.9$. For $U = 6t$, the density is a continuously increasing function of the chemical potential and the system is always found in a metallic state for this value of the interaction. The staggered magnetization is peaked close to integer filling $n = 1$ and it decreases continuously upon particle doping, whereas it vanishes abruptly for hole doping.

At $U = 8t$, the density curve displays a plateau for $n = 1$, which signals the onset of an insulating phase at integer filling. Also in this case, the staggered magnetization jumps to zero in a discontinuous fashion upon hole doping. For moderate

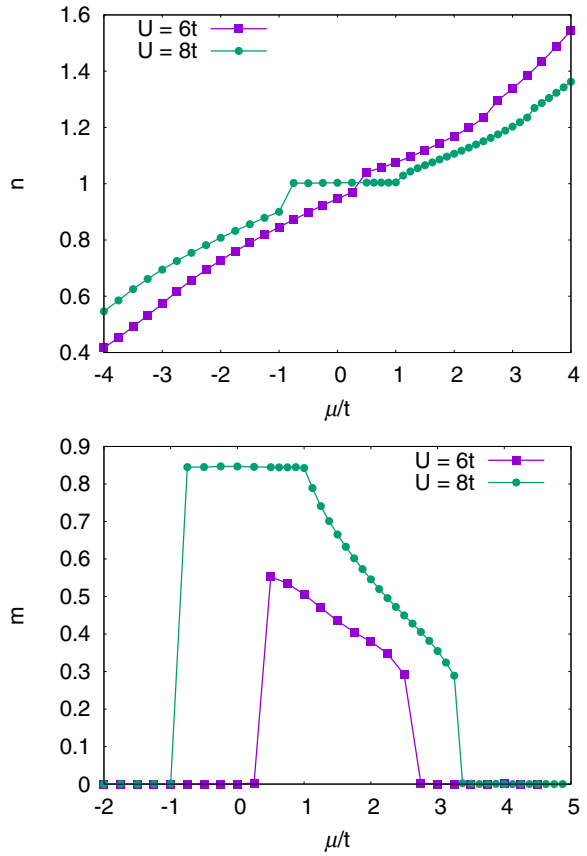


FIG. 4. (Top panel) Density $n = n_{A\uparrow} + n_{A\downarrow}$ as a function of the chemical potential for two values of $U/t = 6, 8$, $t'/t = 0.3$, $\delta = 0.9$, and zero temperature. (Lower panel) Staggered magnetization $m = n_{A\uparrow} - n_{A\downarrow}$ as a function of the chemical potential for the same parameters.

particle doping, the system becomes a magnetic metal and the order parameter decreases to intermediate values before vanishing.

Further insights about the nature of these metallic and insulating states can be grasped by inspection of the single-particle spectral function $A_\sigma(k,\omega) = -\mathrm{Im}\mathrm{Tr}\, G_\sigma(k,\omega + i0^+)$, which is obtained from the analytic continuation of Eq. (6), which in ED can be obtained analytically via Lehmann representation.

The top panels of Fig. 5 show the evolution of the single-particle spectrum as a function of doping for $U/t = 6$ and $\sigma = \uparrow$ plotted as an intensity map in the plane ω versus k. From left to right, the chemical potential is set to $\mu/t = 0.5, 2, 3$. At $\mu = 0.5$, which corresponds to $n \sim 1$, the order parameter assumes its maximal value shown in Fig. 4 (blue curve). We observe that the spectral function displays a linear crossing in the direction (π,π)–$(\pi, 0)$, where, according to Eq. (3), we expect to find a Dirac cone. Furthermore, the spectrum is characterized by the presence of two quasiflat bands, one at higher energy, which we refer to as particle flat band (PFB), and the other at lower energy, which we named hole flat band (HFB). At $\mu/t = 2$, the chemical potential (displayed as a solid white horizontal line) lies below the PFB and the Dirac point is still visible. By further increasing the chemical potential, the altermagnetic state becomes unstable and the Dirac point disappears, as shown in Fig. 5(c). We observe that at $\mu/t = 0.5$, the chemical potential lies slightly above the HFB, and by decreasing doping, the order parameter vanishes, as shown in Fig. 4.

The lower panels of Fig. 5 display the spectral function at $U/t = 8$ for different values of the Fermi level. We note that at $\mu = 0$, which corresponds to integer filling (see Fig. 4), the spectrum is gapped, with a gap of $\tilde{\Delta} \sim 2t$ that coincides with the plateau width of the density curve in Fig. 4. We note that the spectral weight redistributes to higher positive and negative energies forming the Hubbard bands. At $\mu/t = 1.125$ [Fig. 5(e)], the Fermi level is high enough to populate the first low-energy band and the system becomes metallic. However, differently from the AF-metallic phase at $U/t = 6$, the spectrum does not feature any Dirac points and it is similar to the one of a doped Mott insulator. Upon further increasing doping, at $\mu/t = 2$ Dirac cones arise in the spectrum, as shown in Fig. 5(f). For greater values of μ/t, where the symmetric phase is restored, the Dirac points vanish again (not shown).

In order to rationalize the DMFT numerical data, it is useful to derive an effective low-energy theory. For this purpose, we consider a linear expansion in frequency of the self-energy, i.e., $\Sigma_\sigma(\nu) \sim \Sigma_{0\sigma} + \alpha_\sigma i\nu$, where $\Sigma_{0\sigma} = \mathrm{Re}\Sigma_\sigma(\nu \to 0^+)$ and $\alpha_\sigma = \partial_\nu \mathrm{Im}\Sigma_\sigma(\nu)|_{\nu\to 0^+}$. Once this simplified expression of Σ is substituted into Eq. (6), we obtain the following approximation for the Green's function: $G_\sigma^{-1}(k,\nu) \sim Z^{-1/2} \cdot (i\nu - \tilde{\mathcal{H}}_{k\sigma}) \cdot Z^{-1/2}$, where

$$\tilde{\mathcal{H}}_{k\sigma} = Z^{1/2} \cdot (\mathcal{H}_{0\sigma}(k) + \Sigma_0) \cdot Z^{1/2} \tag{7}$$

is the effective QP Hamiltonian, "·" represents matrix multiplication, $\Sigma_0 = \mathrm{diag}(\Sigma_{0\uparrow}, \Sigma_{0\downarrow})$ represents the Hartree term, and $Z = \mathrm{diag}(Z_\uparrow, Z_\downarrow)$, with $Z_\sigma = (1 - \alpha_\sigma)^{-1}$ being the spin/sublattice-resolved QP renormalization factor. If we neglect the spin dependence of the QP weight, the effective Hamiltonian in Eq. (7) coincides with the one defined in Eq. (2) times a prefactor and where $2\Delta = \Sigma_{0\uparrow} - \Sigma_{0\downarrow}$. The bands obtained from diagonlizing the 2×2 matrix in Eq. (7) are shown as white dashed lines in Fig. 5 and they well capture the salient features of the spectral function at low energy. At zero temperature, the Hartree term $2\Delta = \Sigma_\uparrow - \Sigma_\downarrow$ decreases by increasing (decreasing) doping and a Dirac cone at low energy is formed when it becomes lower than the critical value $\Delta_c = 4t'\delta$, as we checked numerically.

2. *The role of temperature*

Since temperature lowers the order parameter, one might expect that it could favor the appearance of Dirac cones in the energy spectrum, similarly to what we have observed at zero temperature as a function of doping.

The upper panels of Fig. 6 show the temperature evolution of the spectrum for $U/t = 8$. Indeed, we observe that, since the Hartree term decreases with temperature, when $\Delta < \Delta_c$ a Dirac cone appears close to the Fermi level and its behavior is well described by the low-energy theory.

However, for higher values of the interaction strength, where a paramagnetic Mott insulating solution already exists, the temperature evolution of the spectrum changes qualitatively even in the broken-symmetry phase. This is shown in the lower panels of Fig. 6 for $U/t = 14$: at low

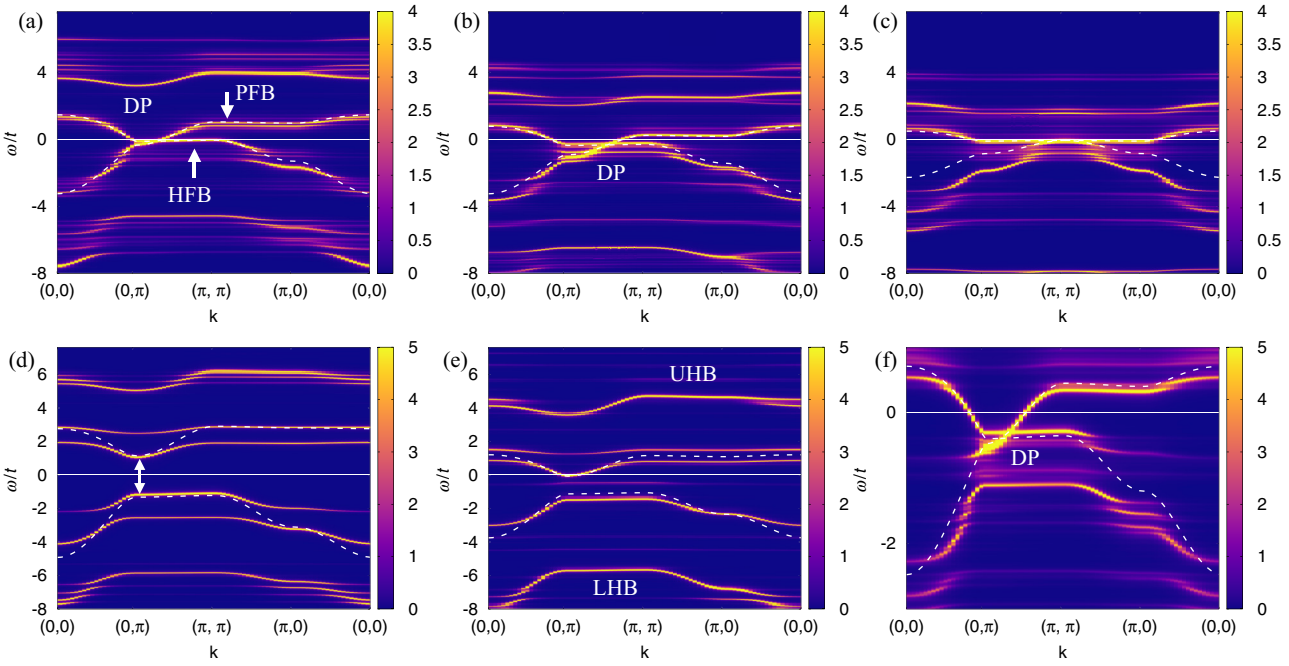


FIG. 5. Doping evolution of the spectrum for two different values of the on-site interaction and for $\sigma = \uparrow$. (Upper panels) $U/t = 6$ and $\mu/t = 0.5,\ 2,\ 3$ for panels (a), (b), and (c), respectively. (Lower panels) $U/t = 8$ and $\mu/t = 0,\ 1.125,\ 2$ for panels (d), (e), and (f), respectively. Dashed lines are predictions from the QP effective theory defined in Eq. (7).

temperature [Fig. 6(d)], the spectrum is fully gapped and no Dirac cones appear. However, for intermediate values of temperature [Fig. 6(e)], we observe that even if the system is still gapped, two Dirac points emerge at high negative and positive energies. These features are completely missed by the effective QP theory and they never appear in mean-field theory.

An alternative approximation to the QP effective theory, which fails at intermediate temperature where dynamical correlations are not negligible anymore, is obtained by evaluating

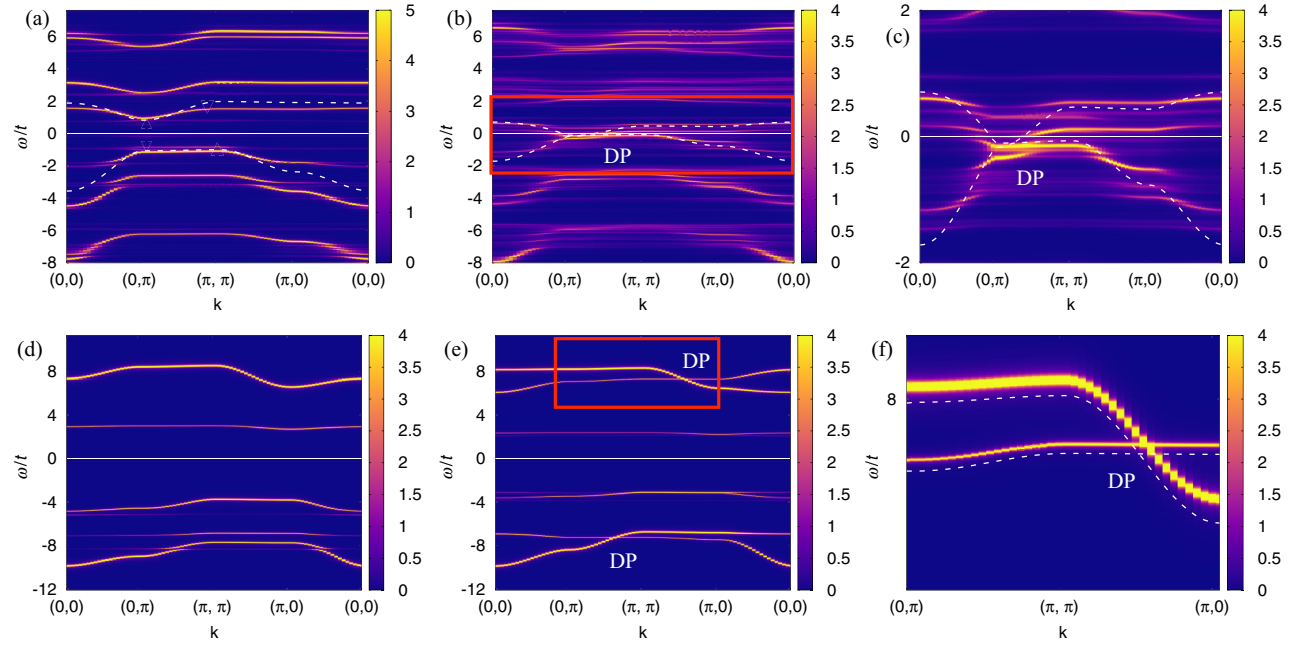


FIG. 6. Temperature evolution of the spectrum for two different values of the interaction and for $\sigma = \uparrow$. (Upper panels) $U/t = 8$ and $\beta t = 5,\ 3.425$ for panels (a) and (b), respectively. Panel (c) is an inset of panel (b). The dashed white lines are the results of the QP effective theory defined in Eq. (7). (Lower panels) $U/t = 14$ and $\beta t = 25,\ 9$ for panels (d) and (e), respectively. Panel (f) is an inset of panel (e). The dashed white lines are the results of the strong coupling expansion based on the approximation presented in Eq. (8) (see main text).

the self-energy in the atomic limit of Eq. (1) in the presence of a finite magnetization, which reads

$$\Sigma_\sigma^{\text{a.l.}}(z) = -\frac{U}{2}\frac{\sigma\, m\, z - (U/2)}{z - \sigma\, m\, (U/2)}, \tag{8}$$

where z represents the frequency in the complex plane. If we substitute Eq. (8) into Eq. (6), we obtain an approximated version of the Green's function that we expect to be valid for large enough interaction strengths. The Green's function poles, which determine the structure of the single-particle spectrum, are given by the zeros of the determinant of Eq. (6), which by fixing $k_x = \pi$ or $k_y = \pi$ simplifies as following:

$$(z - f_A(k) - \Sigma_\uparrow^{\text{a.l.}}(z))(z - f_B(k) - \Sigma_\downarrow^{\text{a.l.}}(z)) = 0. \tag{9}$$

Within this approximation, at $T = 0$, the system is fully polarized and $m = 1$. We observe that, when this limit is considered, the self-energy becomes a real constant $\Sigma_\sigma^{\text{a.l.}}(z, T = 0) = -\sigma(U/2)$ and the system is weakly correlated. In this case, Eq. (9) admits two solutions, $z_{\uparrow(\downarrow)} = \mp U/2 + f_{A(B)}(k)$: the spectrum is fully gapped and the two bands never cross.

However, at finite temperature $m < 1$, the self-energy starts to acquire a nontrivial frequency dependence and Eq. (8) admits four solutions that, when $U \gg f_{A(B)}$, read $z_\uparrow^\pm = [(1 \mp m)/2]f_A \pm U/2$ and $z_\downarrow^\pm = [(1 \pm m)/2]f_B \pm (U/2)$. Crossing for the lower (upper) bands occurs at $k_{y(x)} = \pi$ and $k_{x(y)} = \pm\arccos[(m - \delta)/(m + \delta)]$. Hence, for large values of U, there are two pairs of Dirac points per spin located at different energies. The visibility of the crossing is related to the intensity of the solutions brought by the frequency dependence of the self-energy for $m < 1$, which for the lower (upper) branches is calculated as the residue of the Green's function at $\bar{z} = z_{\uparrow(\downarrow)}^{+(-)}$, which amounts approximately to $\text{Res}G_{AA,\uparrow}|_{z=\bar{z}} \sim (1 - m)/2$. Therefore, at strong coupling, we expect to observe the Hubbard bands crossing more clearly at intermediate temperature/magnetization values, which is confirmed by our numerical calculations.

V. OPTICAL CONDUCTIVITY

Here, we analyze the optical conductivity of the system across different parameter regimes in the limit where the interaction strength is much larger than the hopping amplitude. We consider the system's response to an electric field, introduced as the time derivative of a homogeneous, time-dependent vector potential $\mathbf{A}(t)$. This vector potential enters the model via the Peierls substitution, implemented by modifying the hopping term as $t_{ij} \to t_{ij} e^{i(\mathbf{R}_i - \mathbf{R}_j)\cdot\mathbf{A}(t)}$. Using the Kubo formalism, we derive the following expression for the spin-resolved optical conductivity:

$$\text{Re}\,\sigma_\sigma^{\mu\nu}(\omega + i\eta) = \frac{1}{V}\sum_{\mathbf{k}}\int_{-\infty}^{+\infty} d\omega'\, \Lambda_{k\sigma}^{\mu\nu}(\omega, \omega') F(\omega, \omega'), \tag{10}$$

where $\Lambda_{k\sigma}^{\mu\nu}(\omega, \omega') = \text{Tr}\,[V_k^\mu \cdot \mathcal{A}_k^\sigma(\omega') \cdot V_k^\nu \cdot \mathcal{A}_k^\sigma(\omega' + \omega)]$, with $\mathcal{A}_k^\sigma(\omega) = -\text{Im}\,G_\sigma(k, \omega + i\eta)$ is the 2×2 spectral function matrix, $V_k^\mu = \nabla\mathcal{H}_0(\mathbf{k}) \cdot \hat{e}_\mu$ is the velocity matrix along the μ direction, and $F(\omega, \omega') = [f(\omega') - f(\omega + \omega')]/\omega$, where f being the Fermi-Dirac distribution function. The charge current induced by an electric field is proportional to the sum over spin indices of the quantity in Eq. (10), whereas the spin current is proportional to their difference. Due to symmetry considerations, the off-diagonal components of the conductivity tensor ($\mu \neq \nu$) vanish. However, the diagonal components remain spin dependent, with $\sigma_\sigma^{\mu\mu} \neq \sigma_{\bar{\sigma}}^{\mu\mu}$, and satisfy the relation $\sigma_\sigma^{xx} = \sigma_{\bar{\sigma}}^{yy}$.

The static limit of Eq. (10) has already been studied in the metallic phase in Ref. [29]. In this section, we focus on the dynamical structure of the optical conductivity in the insulating phase. To this end, we evaluate Eq. (10) numerically using the self-energy expression given in Eq. (8), which is appropriate in the strong-coupling regime. Specifically, we set $U/t = 12$, $t'/t = 0.3$, and $\beta t = 10$. For the numerical evaluation of Eq. (10), we used an 80×80 $\mathbf{k}$-point grid and fixed $\eta = 0.05$. We analyze three distinct physical scenarios:

(1) The first case (upper panel of Fig. 7) corresponds to the response to an electric field in a standard antiferromagnetic ground state, obtained by setting $\delta = 0$ and $m = 1$. In this case, the optical conductivity spectrum is peaked around $\omega = U$, as expected for a Mott insulating phase. We also note that the spin-up and spin-down contributions are identical due to Kramers degeneracy.

(2) The second case (central panel of Fig. 7) corresponds to a fully polarized altermagnetic phase, obtained by setting $\delta = 0.9$ and $m = 1$. In this regime, the spin-resolved optical conductivity displays markedly different behavior for the two spin species. Each spectrum is characterized by a single-peaked function, with the maximum located below the interaction energy U for spin-up and above U for spin-down.

(3) The third case (lower panel of Fig. 7) corresponds to a correlated altermagnetic state with intermediate polarization, obtained by setting $m = 0.5$ and $\delta = 0.9$. As discussed in the previous section, the spectral function in this phase features two additional bands crossing the original ones present at full polarization, forming two high-energy Dirac cones located at distinct energies. These more intricate spectral features are reflected in the spin-resolved optical conductivity, which exhibits a characteristic double-peak structure with a pronounced minimum in between.

Let us note that our calculations are valid within the DMFT approximation, which assumes a local self-energy and a local vertex function. In the presence of a momentum-dependent vertex function, one would need to include vertex corrections in the expression for the conductivity, which would likely lead to quantitative modifications of the results reported here [45]. This would considerably complicate the calculation and is beyond the scope of the present work; we leave this for future study.

VI. TOPOLOGICAL PHASE TRANSITION

Adding an appropriate perturbation to the free Hamiltonian, it is possible to obtain bands carrying nontrivial topology [46–48]. Here we shall consider two possibilities: 1 a spin-independent and 2 a spin-dependent complex hopping. In case (1), $\delta\mathcal{H}_\sigma = \sigma^{(y)} g_k$, where $g_k = -2t_c \cos[(k_x - k_y)/2]$. Hence, the Hamiltonian defined in Eq. (2) transforms into $\mathcal{H}_\sigma + \delta\mathcal{H}$ and it has two gapped bands with Chern numbers $\mathcal{C}_\sigma^\pm = \pm\text{sgn}(m\, v_x\, v_y)$, where the massive term reads $m = -2t_c \sin(\bar{k}_y/2)$ (see the Appendix).

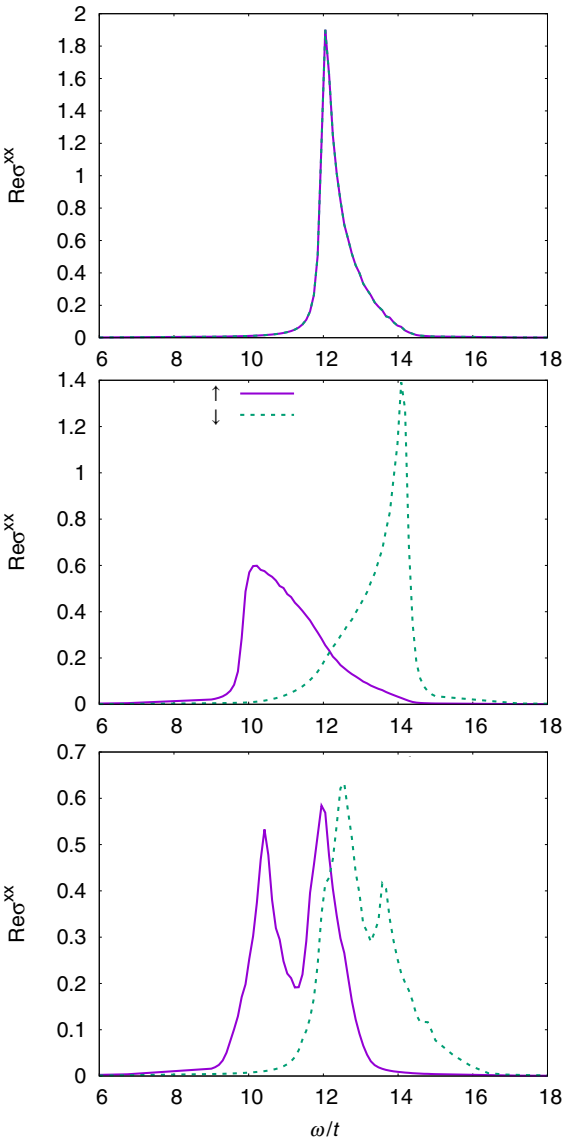


FIG. 7. Spin-up (spin-down) optical conductivity is shown as a thick (dashed) violet (green) line at $U/t = 12$ and $t'/t = 0.3$ for three different cases. Top panel: $m = 1$ and $\delta = 0$—fully polarized standard antiferromagnet. Center panel: $m = 1$ and $\delta = 0.9$—altermagnetic ground state at $T = 0$. Lower panel: $m = 0.5$ and $\delta = 0.9$—correlated altermagnet at finite temperature.

In case 2, we set $\delta\mathcal{H}_\sigma = \sigma^{(y)}\sigma g_k$ and since the hopping sign is spin dependent, the spin-resolved Chern number is now given by $\mathcal{C}_\sigma^{\pm} = \pm\sigma\,\mathrm{sgn}(m\, v_x\, v_y)$.

Since the Chern number is inherently related to the presence of Dirac points in the unperturbed spectrum, the absence of those points will yield trivial topological states. Hence, we expect to observe a topological transition by varying the physical parameters such as doping, temperature, and interaction strength. For example, in Fig. 8 we show the effective bands extracted from our DMFT numerical results for two values of temperature at intermediate coupling: at zero temperature, the system is gapped and the bands are topologically trivial, while for a high enough value of temperature, the bands carry a nonzero Chern number.

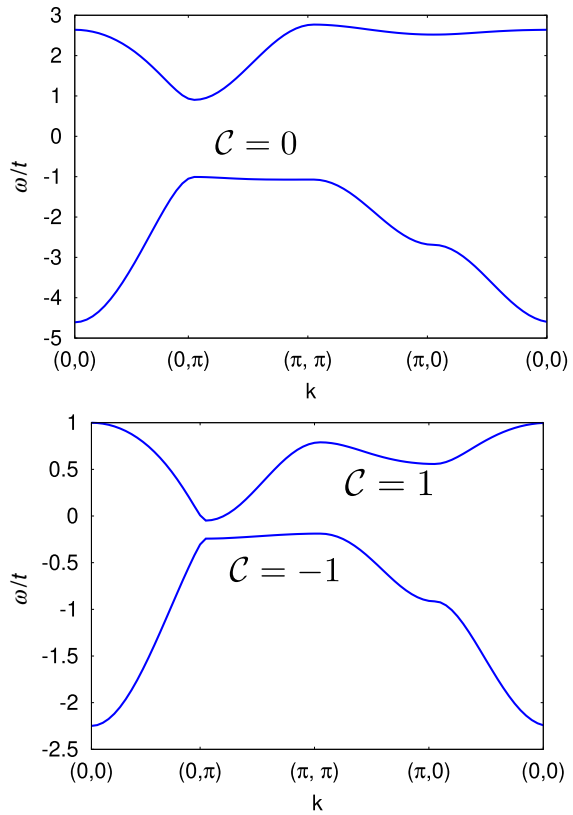


FIG. 8. Effective bands calculated with DMFT for $U/t = 8$, $t_c/t = 0.5$, $t'/t = 0.3$, and $\delta = 0.9$ at zero temperature (top panel) and at $\beta t = 3.425$ (lower panel).

VII. CONCLUSIONS

We have theoretically and numerically investigated altermagnetic states arising from a suitably modified Hubbard model. HF predicts a transition from an altermagnetic metallic state hosting Dirac cones to an insulating gapped state by increasing the Hartree term, which is controlled by the order parameter. Hence, we demonstrated that a transition from a non-Dirac gapped state to a Dirac magnetic metal can be obtained by doping the system and/or decreasing the interaction strength and/or increasing the temperature. DMFT confirms the HF predictions at zero temperature for all values of the interaction strength, and at finite temperature for moderate values of U.

At finite temperature and at strong coupling, DMFT predicts the emergence of an insulating magnetic state displaying Dirac cones at high energy: These correlated insulating solutions are characterized by a strong frequency dependence of the self-energy and they cannot be described by a static-mean-field ansatz. Since the Dirac points tend to be activated by temperature for a wide range of interaction values, we expect that these states could be stabilized in cold-atom systems where thermal fluctuations play a central role.

In the insulating regime, we analyzed the spin-resolved optical conductivity under finite temperature and strong electronic correlations, focusing on altermagnetic states with varying polarization. Using the Kubo formalism combined with Peierls substitution, we numerically evaluated the

conductivity tensor in the strong-coupling limit. Our findings highlight distinct dynamical features: A spin-dependent single-peak structure in the fully polarized altermagnet and a characteristic double-peak structure with a pronounced minimum in the intermediate polarization regime. This complex behavior appears linked to the emergence of additional high-energy bands, associated with Dirac conelike features in the spectral function, illustrating the subtle interplay between electronic correlations and altermagnetic order. Moreover, we observe that the optical conductivity for spin-up and spin-down electrons is asymmetrically distributed: The spin-up response is shifted toward lower energies, while the spin-down response appears at higher energies relative to the interaction scale U. This implies that the two spin channels are activated at different photon energies, suggesting a form of spin-selective optical excitation. Such a mechanism could be exploited for spin-dependent optical filtering or detection, potentially opening avenues for technological applications in spintronic or optoelectronic devices based on correlated materials. Since our analysis is restricted to the linear response regime, we did not explore the real-time evolution of the altermagnetic state under an applied electric field. Investigating such nonequilibrium dynamics [49] within our model would be an interesting direction for future work.

Finally, we showed how the Dirac points can be gapped by suitable perturbations to the original Hamiltonian, inducing topological phase transitions as a function of the physical parameters. Given the bulk-edge correspondence [50], a topological transition in the bulk will be accompanied by the emergence of edge states on the surface, which can be detected in a cold-atomic experiment [51–54].

Extension of DMFT such as diagrammatic [55] and cluster theories [56] could be used to investigate the topological properties of the Green's function zeros when these acquire a nontrivial dependence on the crystalline momentum [57–59].

The extension of this model to bilayer altermagnetic systems [60–64] suggests that it offers a promising platform for the emergence of unconventional superconductivity [35] and for spintronics applications, notably enabling spin transport even in Mott insulating states [65].

Our results demonstrate that the physics emerging from this model is rich, lying at the intersection of quantum magnetism, strongly correlated systems, Dirac materials [66,67], and topology. Its realization represents an ideal target for quantum simulators, particularly in the context of cold atoms trapped in optical lattices.

ACKNOWLEDGMENT

I thank Andreas Schnyder, Kirill Parshukov, Raymond Wiedmann, Laura Classen, Giorgio Sangiovanni, and Alessandro Toschi for valuable discussions.

DATA AVAILABILITY

The numerical data supporting the findings of this study are available from the corresponding author upon reasonable request.

APPENDIX: TOPOLOGICAL INVARIANTS

Let us consider the following 2×2 Hamiltonian:

$$\mathcal{H}_\sigma(k) = \alpha_k \mathbb{I}_{2\times 2} + \beta_{k\sigma}\sigma^{(z)} + \gamma_k \sigma^{(x)} + \lambda_{k\sigma}\sigma^{(y)}. \tag{A1}$$

The eigenvalues of this Hamiltonian are given by $\alpha_k \pm \rho_{k\sigma}$, where $\rho_{k\sigma} = \sqrt{\beta_{k\sigma}^2 + \gamma_k^2 + \lambda_{k\sigma}^2}$ and eigenvectors

$$|\pm, k, \sigma\rangle = \frac{1}{\sqrt{\rho_{k\sigma}(\rho_{k\sigma} \pm \beta_{k\sigma})}} \begin{pmatrix} \beta_{k\sigma} \pm \rho_{k\sigma} \\ \gamma_k + i\lambda_{k\sigma} \end{pmatrix}. \tag{A2}$$

1. Numerical evaluation of the Chern number

The Chern number for the nth band can then be calculated as

$$\mathcal{C}_\sigma^{(n)} = \frac{1}{2\pi} \sum_k F_{k\sigma}^{(n)}, \tag{A3}$$

where

$$F_{k\sigma}^{(n)} = -\mathrm{Im} \ln U_{k\to k_1,\sigma}^{(n)} U_{k_1\to k_2,\sigma}^{(n)} U_{k_2\to k_3,\sigma}^{(n)} U_{k_3\to k,\sigma}^{(n)}, \tag{A4}$$

with $k_1 = k + (2\pi/N, 0)$, $k_2 = k + (2\pi/N, 2\pi/N)$, $k_3 = k + (0, 2\pi/N)$, $U_{k\to k',\sigma}^{(n)} = \langle n, k, \sigma | n, k', \sigma \rangle$, and $n = \pm$ [68–70].

In DMFT, we can calculate the Chern number from the renormalized QP Hamiltonian [57]:

$$\mathcal{H}_{k\sigma} = Z^{1/2} \cdot (\mathcal{H}_{0\sigma}(k) + \Sigma_0) \cdot Z^{1/2}, \tag{A5}$$

where $\Sigma_0 = \mathrm{diag}(\Sigma_{0\uparrow}, \Sigma_{0\downarrow})$ represents the Hartree term, $Z = \mathrm{diag}(Z_\uparrow, Z_\downarrow)$, with $Z_\sigma = (1 - \alpha_\sigma)^{-1}$ being the spin/sublattice-resolved QP renormalization factor. Let us now fix the noninteracting Hamiltonian to the perturbed one introduced in the last section in the main text, i.e.,

$$\mathcal{H}_{0\sigma}(k) = \begin{pmatrix} f_A(k) & \epsilon_k - i\, g_{k\sigma} \\ \epsilon_k + i\, g_{k\sigma} & f_B(k) \end{pmatrix}. \tag{A6}$$

As mentioned in Sec. VI, we consider two possible cases: (1) $g_{k\sigma} = -2t_c \cos[(k_x - k_y)/2]$, where the perturbation is spin independent, and (2) $g_{k\sigma} = -2\sigma t_c \cos[(k_x - k_y)/2]$, where the sign of the perturbation depends on the spin index.

We observe that even if in single-site DMFT the self-consistency condition is the same in these two cases, the topology of the band structure is sensitive to the spin-dependent sign change.

2. Low-energy Hamiltonian

We can expand the perturbed Hamiltonian for the two different spin species in the proximity of the Dirac points:

$$\begin{aligned} \mathcal{H}_\uparrow^\pm &= v_x q_x \sigma^{(x)} \pm v_z q_y \sigma^{(z)} \pm m_\uparrow \sigma^{(y)}, \\ \mathcal{H}_\downarrow^\pm &= v_x q_y \sigma^{(x)} \mp v_z q_x \sigma^{(z)} \pm m_\downarrow \sigma^{(y)}, \end{aligned} \tag{A7}$$

where $v_x = 2t\cos(\bar{k}/2)$ and $v_y = -2t'\delta\sin(\bar{k})$, with $\bar{k} = \arccos[(\Delta/2t'\delta) - 1]$, $\mathbf{q} = (k_x - \pi, k_y \mp \bar{k})$ for $\sigma = \uparrow$, $\mathbf{q} = (k_y \mp \bar{k}, k_x - \pi)$ for $\sigma = \downarrow$, and where we omitted the part proportional to the identity matrix. The massive term proportional to $\sigma^{(y)}$ can be spin dependent or spin independent

according to the kind of perturbation added. In case (1), $m_\sigma = m = -2t_c \sin(\bar{k}/2)$, while for case (2), $m_\sigma = \sigma\, m$. The Berry connection for the conduction band is defined as $\mathbf{A}^s(\mathbf{q}) = \langle +, \mathbf{q}, \sigma, s | i\,\nabla | +, \mathbf{q}, \sigma, s \rangle$, where we added the index $s = \pm$ that specifies a particular Dirac point. Hence, the Chern number for the conduction band is given by

$$\mathcal{C}_\sigma^+ = \sum_s \frac{1}{2\pi} \int d\mathbf{q}\, \partial_x A_y^s(\mathbf{q}) - \partial_y A_x^s(\mathbf{q}) = \mathrm{sgn}(m_\sigma\, v_x\, v_y). \tag{A8}$$

[1] Y. Noda, K. Ohno, and S. Nakamura, Momentum-dependent band spin splitting in semiconducting MnO_2: A density functional calculation, Phys. Chem. Chem. Phys. **18**, 13294 (2016).

[2] K.-H. Ahn, A. Hariki, K.-W. Lee, and J. Kuneš, Antiferromagnetism in RuO_2 as d-wave Pomeranchuk instability, Phys. Rev. B **99**, 184432 (2019).

[3] I. Mazin *et al.*, Prediction of unconventional magnetism in doped $FeSb_2$, Proc. Natl. Acad. Sci. USA **118**, e2108924118 (2021).

[4] I. Mazin (The PRX Editors), Editorial: Altermagnetism—A new punch line of fundamental magnetism, Phys. Rev. X **12**, 040002 (2022).

[5] L. Šmejkal, J. Sinova, and T. Jungwirth, Beyond conventional ferromagnetism and antiferromagnetism: A phase with nonrelativistic spin and crystal rotation symmetry, Phys. Rev. X **12**, 031042 (2022).

[6] L. Šmejkal, J. Sinova, and T. Jungwirth, Emerging research landscape of altermagnetism, Phys. Rev. X **12**, 040501 (2022).

[7] P. A. McClarty and J. G. Rau, Landau theory of altermagnetism, Phys. Rev. Lett. **132**, 176702 (2024).

[8] H. Schiff, A. Corticelli, A. Guerreiro, J. Romhányi, and P. A. McClarty, The crystallographic spin point groups and their representations, SciPost Phys. **18**, 109 (2025).

[9] P. Wadley *et al.*, Electrical switching of an antiferromagnet, Science **351**, 587 (2016).

[10] V. Baltz, A. Manchon, M. Tsoi, T. Moriyama, T. Ono, and Y. Tserkovnyak, Antiferromagnetic spintronics, Rev. Mod. Phys. **90**, 015005 (2018).

[11] H. Bai, L. Han, X. Y. Feng, Y. J. Zhou, R. X. Su, Q. Wang, L. Y. Liao, W. X. Zhu, X. Z. Chen, F. Pan, X. L. Fan, and C. Song, Observation of spin splitting torque in a collinear antiferromagnet RuO_2, Phys. Rev. Lett. **128**, 197202 (2022).

[12] A. Hariki, A. Dal Din, O. J. Amin, T. Yamaguchi, A. Badura, D. Kriegner, K. W. Edmonds, R. P. Campion, P. Wadley, D. Backes, L. S. I. Veiga, S. S. Dhesi, G. Springholz, L. Šmejkal, K. Výborný, T. Jungwirth, and J. Kuneš, X-ray magnetic circular dichroism in altermagnetic α-MnTe, Phys. Rev. Lett. **132**, 176701 (2024).

[13] J. Krempaský *et al.*, Altermagnetic lifting of Kramers spin degeneracy, Nature (London) **626**, 517 (2024).

[14] Y.-P. Zhu, X. Chen, X.-R. Liu, Y. Liu, P. Liu, H. Zha, G. Qu, C. Hong, J. Li, Z. Jiang *et al.*, Observation of plaid-like spin splitting in a noncoplanar antiferromagnet, Nature (London) **626**, 523 (2024).

[15] B. Jiang *et al.*, A metallic room-temperature d-wave altermagnet, Nat. Phys. **21**, 754 (2025).

[16] R. B. Regmi, H. Bhandari, B. Thapa, Y. Hao, N. Sharma, J. McKenzie, X. Chen, A. Nayak, M. El Gazzah, B. G. Márkus *et al.*, Altermagnetism in the layered intercalated transition metal dichalcogenide $CoNb_4Se_8$, Nat. Commun. **16**, 4399 (2025).

[17] A. D. Vita *et al.*, Optical switching in a layered altermagnet, arXiv:2502.20010.

[18] M. Naka, Y. Motome, and H. Seo, Altermagnetic perovskites, npj Spintronics **3**, 1 (2025).

[19] X. Gong, A. Fakhredine, and C. Autieri, Tunability of the magnetic properties in Ni intercalated transition metal dichalcogenide $NbSe_2$, arXiv:2505.17916.

[20] S. V. Streltsov and D. M. Korotin, Altermagnetism and anomalous Hall effect in $LaMn_2Si_2$, arXiv:2507.23233.

[21] R. Jördens, N. Strohmaier, K. Günter, H. Moritz, and T. Esslinger, A Mott insulator of fermionic atoms in an optical lattice, Nature (London) **455**, 204 (2008).

[22] T. Esslinger, Fermi-Hubbard physics with atoms in an optical lattice, Annu. Rev. Condens. Matter Phys. **1**, 129 (2010).

[23] S. Taie, R. Yamazaki, S. Sugawa, and Y. Takahashi, An SU(6) Mott insulator of an atomic Fermi gas realized by large-spin Pomeranchuk cooling, Nat. Phys. **8**, 825 (2012).

[24] D. Tusi, L. Franchi, L. Livi, K. Baumann, D. Benedicto Orenes, L. Del Re, R. Barfknecht, T.-W. Zhou, M. Inguscio, G. Cappellini *et al.*, Flavour-selective localization in interacting lattice fermions, Nat. Phys. **18**, 1201 (2022).

[25] R. A. Hart, P. M. Duarte, T.-L. Yang, X. Liu, T. Paiva, E. Khatami, R. T. Scalettar, N. Trivedi, D. A. Huse, and R. G. Hulet, Observation of antiferromagnetic correlations in the Hubbard model with ultracold atoms, Nature (London) **519**, 211 (2015).

[26] A. Mazurenko, C. S. Chiu, G. Ji, M. F. Parsons, M. Kanász-Nagy, R. Schmidt, F. Grusdt, E. Demler, D. Greif, and M. Greiner, A cold-atom Fermi-Hubbard antiferromagnet, Nature (London) **545**, 462 (2017).

[27] M. Xu, L. H. Kendrick, A. Kale, Y. Gang, G. Ji, R. T. Scalettar, M. Lebrat, and M. Greiner, Frustration- and doping-induced magnetism in a Fermi-Hubbard simulator, Nature (London) **620**, 971 (2023).

[28] H.-J. Shao, Y.-X. Wang, D.-Z. Zhu, Y.-S. Zhu, H.-N. Sun, S.-Y. Chen, C. Zhang, Z.-J. Fan, Y. Deng, X.-C. Yao *et al.*, Antiferromagnetic phase transition in a 3D fermionic Hubbard model, Nature (London) **632**, 267 (2024).

[29] P. Das, V. Leeb, J. Knolle, and M. Knap, Realizing altermagnetism in Fermi-Hubbard models with ultracold atoms, Phys. Rev. Lett. **132**, 263402 (2024).

[30] A. Georges, G. Kotliar, W. Krauth, and M. J. Rozenberg, Dynamical mean-field theory of strongly correlated fermion systems and the limit of infinite dimensions, Rev. Mod. Phys. **68**, 13 (1996).

[31] F. D. M. Haldane, Model for a quantum Hall effect without Landau levels: Condensed-matter realization of the "parity anomaly", Phys. Rev. Lett. **61**, 2015 (1988).

[32] C. L. Kane and E. J. Mele, Quantum spin Hall effect in graphene, Phys. Rev. Lett. **95**, 226801 (2005).

[33] X.-L. Qi, Y.-S. Wu, and S.-C. Zhang, Topological quantization of the spin Hall effect in two-dimensional paramagnetic semiconductors, Phys. Rev. B **74**, 085308 (2006).

[34] M. Z. Hasan and C. L. Kane, *Colloquium:* Topological insulators, Rev. Mod. Phys. **82**, 3045 (2010).

[35] J. Chang, H. Lu, J. Zhao, H.-G. Luo, and Y. Ding, Energy dispersion, superconductivity, and magnetic fluctuations in stacked altermagnetic materials, Phys. Rev. B **111**, 104432 (2025).

[36] S. He, J. Zhao, H.-G. Luo, and S. Hu, Altermagnetism and beyond in the $t-t'-\delta$ Fermi-Hubbard model, Phys. Rev. B **112**, 035108 (2025).

[37] M. Milićević, G. Montambaux, T. Ozawa, O. Jamadi, B. Real, I. Sagnes, A. Lemaître, L. Le Gratiet, A. Harouri, J. Bloch, and A. Amo, Type-III and tilted Dirac cones emerging from flat bands in photonic orbital graphene, Phys. Rev. X **9**, 031010 (2019).

[38] G. Sangiovanni, A. Toschi, E. Koch, K. Held, M. Capone, C. Castellani, O. Gunnarsson, S.-K. Mo, J. W. Allen, H.-D. Kim, A. Sekiyama, A. Yamasaki, S. Suga, and P. Metcalf, Static versus dynamical mean-field theory of Mott antiferromagnets, Phys. Rev. B **73**, 205121 (2006).

[39] L. Del Re and G. Rohringer, Fluctuations analysis of spin susceptibility: Néel ordering revisited in dynamical mean field theory, Phys. Rev. B **104**, 235128 (2021).

[40] L. Del Re and A. Toschi, Dynamical vertex approximation for many-electron systems with spontaneously broken SU(2) symmetry, Phys. Rev. B **104**, 085120 (2021).

[41] M. Reitner, L. D. Re, M. Capone, and A. Toschi, Non-perturbative feats in the physics of correlated antiferromagnets, arXiv:2411.13417.

[42] L. Del Re, Two-particle self-consistent approach for broken symmetry phases, SciPost Phys. **18**, 077 (2025).

[43] S. Giuli, C. Mejuto-Zaera, and M. Capone, Altermagnetism from interaction-driven itinerant magnetism, Phys. Rev. B **111**, L020401 (2025).

[44] See Refs. [71–73] for more technical details on ED-DMFT.

[45] T. Sato and H. Tsunetsugu, Cluster dynamical mean field theory study of antiferromagnetic transition in the square-lattice Hubbard model: Optical conductivity and electronic structure, Phys. Rev. B **94**, 085110 (2016).

[46] K. Parshukov, R. Wiedmann, and A. P. Schnyder, Topological crossings in two-dimensional altermagnets: Symmetry classification and topological responses, Phys. Rev. B **111**, 224406 (2025).

[47] Z. Meng-Han, G. Xuan, and D.-X. Yao, Dirac points and Weyl phase in a honeycomb altermagnet, arXiv:2412.03657.

[48] D. S. Antonenko, R. M. Fernandes, and J. W. F. Venderbos, Mirror Chern bands and Weyl nodal loops in altermagnets, Phys. Rev. Lett. **134**, 096703 (2025).

[49] A. Eskandari-asl, J. I. Facio, O. Janson, A. Avella, and J. van den Brink, Controlling photoexcited electron spin by light polarization in ultrafast-pumped altermagnets, Phys. Rev. B **112**, 024401 (2025).

[50] G. M. Graf and M. Porta, Bulk-edge correspondence for two-dimensional topological insulators, Commun. Math. Phys. **324**, 851 (2013).

[51] M. Mancini, G. Pagano, G. Cappellini, L. Livi, M. Rider, J. Catani, C. Sias, P. Zoller, M. Inguscio, M. Dalmonte, and L. Fallani, Observation of chiral edge states with neutral fermions in synthetic Hall ribbons, Science **349**, 1510 (2015).

[52] B. K. Stuhl, H.-I. Lu, L. M. Aycock, D. Genkina, and I. B. Spielman, Visualizing edge states with an atomic Bose gas in the quantum Hall regime, Science **349**, 1514 (2015).

[53] T. Chalopin, T. Satoor, A. Evrard, V. Makhalov, J. Dalibard, R. Lopes, and S. Nascimbene, Probing chiral edge dynamics and bulk topology of a synthetic Hall system, Nat. Phys. **16**, 1017 (2020).

[54] C. Braun, R. Saint-Jalm, A. Hesse, J. Arceri, I. Bloch, and M. Aidelsburger, Real-space detection and manipulation of topological edge modes with ultracold atoms, Nat. Phys. **20**, 1306 (2024).

[55] G. Rohringer, H. Hafermann, A. Toschi, A. A. Katanin, A. E. Antipov, M. I. Katsnelson, A. I. Lichtenstein, A. N. Rubtsov, and K. Held, Diagrammatic routes to nonlocal correlations beyond dynamical mean field theory, Rev. Mod. Phys. **90**, 025003 (2018).

[56] T. Maier, M. Jarrell, T. Pruschke, and M. H. Hettler, Quantum cluster theories, Rev. Mod. Phys. **77**, 1027 (2005).

[57] A. Blason and M. Fabrizio, Unified role of Green's function poles and zeros in correlated topological insulators, Phys. Rev. B **108**, 125115 (2023).

[58] N. Wagner, L. Crippa, A. Amaricci, P. Hansmann, M. Klett, E. König, T. Schäfer, D. D. Sante, J. Cano, A. Millis *et al.*, Mott insulators with boundary zeros, Nat. Commun. **14**, 7531 (2023).

[59] E. A. Stepanov, M. Chatzieleftheriou, N. Wagner, and G. Sangiovanni, Interconnected renormalization of Hubbard bands and Green's function zeros in Mott insulators induced by strong magnetic fluctuations, Phys. Rev. B **110**, L161106 (2024).

[60] S. Zeng and Y.-J. Zhao, Bilayer stacking *a*-type altermagnet: A general approach to generating two-dimensional altermagnetism, Phys. Rev. B **110**, 174410 (2024).

[61] B. Pan, P. Zhou, P. Lyu, H. Xiao, X. Yang, and L. Sun, General stacking theory for altermagnetism in bilayer systems, Phys. Rev. Lett. **133**, 166701 (2024).

[62] E. W. Hodt and J. Linder, Spin pumping in an altermagnet/normal-metal bilayer, Phys. Rev. B **109**, 174438 (2024).

[63] Y. Qi, J. Zhao, and H. Zeng, Spin-layer coupling in two-dimensional altermagnetic bilayers with tunable spin and valley splitting properties, Phys. Rev. B **110**, 014442 (2024).

[64] H. Zeng, W. Zhang, C. Qiu, D.-Z. Ding, and J. Zhao, Symmetry breaking induced nonrelativistic spin splitting and spontaneous valley polarization in altermagnetic $Ca(CoN)_2$ bilayer, Appl. Phys. Lett. **126**, 202405 (2025).

[65] N. Sicheler, R. Raimondi, G. Sangiovanni, and L. D. Re, Optically tunable spin transport in bilayer altermagnetic Mott insulators, arXiv:2508.06938.

[66] T. O. Wehling, A. M. Black-Schaffer, and A. Balatsky, Dirac materials, Adv. Phys. **63**, 1 (2014).

[67] O. Vafek and A. Vishwanath, Dirac fermions in solids: From high-T_c cuprates and graphene to topological insulators and Weyl semimetals, Annu. Rev. Condens. Matter Phys. **5**, 83 (2014).

[68] R. Zhao, G.-D. Xie, M. L. N. Chen, Z. Lan, Z. Huang, and W. E. I. Sha, First-principle calculation of Chern number in gyrotropic photonic crystals, Opt. Express **28**, 4638 (2020).

[69] A. Yamamoto, Berry phase in lattice QCD, Phys. Rev. Lett. **117**, 052001 (2016).

[70] Let us note that the equation for $F^{(n)}_{k\sigma}$ differs from the one in Ref. [68] by a minus sign because we defined the Berry connection as $A_k = \langle\psi_k|i\nabla|\psi_k\rangle$.

[71] M. Capone, L. de' Medici, and A. Georges, Solving the dynamical mean-field theory at very low temperatures using the Lanczos exact diagonalization, Phys. Rev. B **76**, 245116 (2007).

[72] L. Del Re and M. Capone, Selective insulators and anomalous responses in three-component fermionic gases with broken SU(3) symmetry, Phys. Rev. A **98**, 063628 (2018).

[73] M. Ferraretto, A. Richaud, L. D. Re, L. Fallani, and M. Capone, Enhancement of chiral edge currents in $(d + 1)$-dimensional atomic Mott-band hybrid insulators, SciPost Phys. **14**, 048 (2023).